Two-dimensional stimulated resonance Raman spectroscopy of molecules with broadband x-ray pulses

Jason D. Biggs, Yu Zhang, Daniel Healion, and Shaul Mukamel[a]
Department of Chemistry, University of California, Irvine, California 92697-2025, USA

Expressions for the two-dimensional stimulated x-ray Raman spectroscopy (2D-SXRS) signal obtained using attosecond x-ray pulses are derived. The 1D- and 2D-SXRS signals are calculated for trans-N-methyl acetamide (NMA) with broad bandwidth (181 as, 14.2 eV FWHM) pulses tuned to the oxygen and nitrogen K-edges. Crosspeaks in 2D signals reveal electronic Franck-Condon overlaps between valence orbitals and relaxed orbitals in the presence of the core-hole. © *2012 American Institute of Physics*. [http://dx.doi.org/10.1063/1.4706899]

I. INTRODUCTION

Driven by the development of highly intense attosecond sources of x-ray radiation,[1] there is much interest in mapping nonlinear spectroscopic techniques developed for the NMR, IR, and visible regimes to x-ray frequencies.[2,3] These techniques use sequences of laser pulses with well-defined inter-pulse delays to probe the correlation between different nuclear spin, vibrational, or electronic molecular eigenstates. One-dimensional stimulated Raman x-ray spectroscopy (1D-SXRS) has been proposed to prepare and probe valence electronic wavepackets during a delay between two pulses.[4] We present the two-dimensional stimulated x-ray Raman spectroscopy (2D-SXRS) technique, an extension of 1D-SXRS which may be used to probe molecular valence electronic excitations in greater detail. First we briefly survey the optical domain, time-resolved, stimulated Raman experiments which inspire these new x-ray techniques. We will then discuss the dynamics probed by the time and frequency domain x-ray spectroscopies, including 2D-SXRS.

Resonances are observed in optical or ultraviolet Raman spectroscopy when the difference frequency $\omega_1 - \omega_2$ of the incident (ω_1) and scattered (ω_2) field modes match a vibrational transition frequency.[5,6] This inelastic scattering process can be either spontaneous or stimulated by a second interaction with the applied field.[7–9] Femtosecond lasers with bandwidths comparable to molecular vibrational frequencies (on the order of hundreds of wavenumbers) have made it possible to excite vibrations impulsively.[10–13] The dynamics of a slow vibrational system are probed through a perturbation that depends on its coupling to a fast electronic system.[10,14,15] Time-domain vibrational Raman spectroscopy with picosecond delays between pulses was developed in the 1970s (Ref. 9) and used to probe vibrational dephasing. The impulsive pump-probe technique[11–13,16] is one-dimensional (1D) since a single delay time is controlled. Selecting a specific intermediate electronic state by tuning the central frequencies of the exciting pulses determines a unique effective nuclear perturbation during the Raman process.

Multidimensional time-domain stimulated Raman spectroscopies extend these techniques to multiple time evolution periods. Fifth-order off-resonant stimulated Raman spectroscopy was first proposed to examine the vibrational structure in liquids.[17]

These nonlinear techniques were developed in parallel with technological progress in the coherence and intensity of ultrafast lasers. A new generation of very intense ultrafast x-ray sources allow weak nonlinear x-ray transitions to be observed for the first time despite the low cross-section and short lifetimes of core-excitations. X-ray free electron lasers (XFELs) (Ref. 18) convert the kinetic energy of a beam of accelerated electrons to an electromagnetic field by passing the beam through a magnetic grating.[19] The Linac Coherent Light Source (LCLS) at Stanford[20,21] is a next generation XFEL capable of generating extremely intense ($\sim 10^{13}$ photons) pulses with x-ray central frequencies (560−2660 eV),[1] and has already been used to probe exotic forms of plasma[22] and to find the structure of biological samples from a succession of single protein x-ray diffraction snapshots.[23,24] The source is intense enough to create hollow atoms by depopulating both core orbitals for a resonant transition within the Auger decay time of the core-hole in atomic[25] and molecular[26] systems. One drawback of XFEL radiation is that the coherence time is short (<5 fs),[27] a consequence of quantum statistics in the electron bunch used to generate the pulse. Despite this drawback, the high intensity of the LCLS XFEL source make it the most likely candidate for exciting nonlinear x-ray transitions. The technology needed to create pulses with desired characteristics is rapidly improving; an XFEL pumped x-ray laser was recently demonstrated, capable of generating intense, temporally coherent x-ray pulses.[28] Similar advances promise to significantly extend the capability of the LCLS.

Pump-probe and stimulated Raman techniques were among the first nonlinear experiments performed in the visible regime.[7–9,29] This paper focuses on x-ray analogues of multidimensional stimulated Raman techniques, using soft or hard x-ray pulses with bandwidths greater than 10 eV to create wavepackets of electronic excitations. The x-ray interaction involves single particle, field driven, transitions

[a]Electronic mail: smukamel@uci.edu.

between core and valence electronic orbitals and the many-body valence response to a transiently created core-hole.[30] Extensive theoretical[31] and experimental[32] work was applied toward using this unique source as a probe in time-dependent experiments. The low cross-section of the x-ray matter interaction make IR and optical pump/x-ray probe experiments more accessible than the all-x-ray pump-probe technique. IR pump/x-ray probe experiments were proposed and simulated for diatomic molecules.[33–36] Time-resolved optical pump/x-ray probe experiments[37] have been performed at the LCLS which highlight the experimental difficulties in synchronizing pump and probe pulses.[32] All-x-ray stimulated Raman experiments in which the pump and probe pulses both have x-ray frequencies are a natural extension of these techniques. Frequency-domain resonant inelastic x-ray scattering (RIXS) is a well established technique that probes the single-particle occupied and unoccupied density of states around the resonant core by measuring the energy-resolved x-ray radiation spontaneously emitted by a core-excited state.[38,39] An x-ray photon is absorbed, exciting a core electron to an empty (virtual) orbital, and an electron drops into the core-hole, emitting a photon. Peaks in the Fourier transform of the time-domain 1D-SXRS (Ref. 40) signal represent excitations of valence electronic states generated through a core-excited intermediate. Ultrashort x-ray pulses are difficult to manipulate[41] and the cross-section for core-excitation is lower than for excitations at lower frequencies. The feasibility of stimulated and coherent Raman experiments using the LCLS was explored,[42] and schemes for tailoring the electron bunches to generate pairs of attosecond pulses suited for stimulated x-ray Raman experiments have been suggested.[43]

Simulations[44] and experiments[45] suggest that electron correlation can drive charge migration in ionized electronic systems. Thanks to the elemental specificity of resonant x-ray excitation, it can be used as a perturbation that is local in time and space, making nonlinear x-ray spectroscopies attractive for measuring ultrafast dynamics with high spatial resolution. Nonlinear effects in the propagation of XUV pulses,[46] and

atomic attosecond electronic dynamics,[47] were investigated in noble gases, and show that nonlinear effects contribute to measurements using XFEL sources. The 1D-SXRS signal can be expressed as the time-dependent overlap of an impulsively excited valence electron doorway wavepacket with a stationary window created by the probe. SXRS was proposed to investigate the electronic properties of molecules,[40] and applied to conjugated π-bonded organic molecules[4] and excitonic systems[48] using a tight-binding model Hamiltonian. Several extensions and refinements of 1D-SXRS were proposed, including the use of attosecond pulses to prepare entangled particle-hole states,[49] frequency domain coherent anti-Stokes Raman spectroscopy with wide- and narrow-band pulses,[50] and a many-body Green's function-based method suitable for calculating the SXRS of larger systems.[51] X-ray spectra of molecules with cores separated from each other at some distance were discussed.[52]

This paper extends the formalism previously applied to 1D-SXRS to two dimensions (2D-SXRS) by adding one more pulse. Expressions for the 1D-SXRS and 2D-SXRS signals are presented in Secs. II and III, respectively. Simulations of the UV, 1D and 2D-SXRS signals for the nitrogen and oxygen K edges in trans-NMA are reported in Sec. IV, and their significance is discussed in Sec. V.

II. ULTRAFAST ONE DIMENSIONAL STIMULATED RAMAN: 1D-SXRS

1D-SXRS is the simplest time-domain, x-ray Raman technique. The electric field is represented as

$$E(\mathbf{r}, t) = \mathbf{e}_1 \mathcal{E}_1(t) \exp(i\mathbf{k}_1 \cdot \mathbf{r} - i\omega_1 t) + \mathbf{e}_2 \mathcal{E}_2(t - \tau)$$
$$\times \exp(i\mathbf{k}_2 \cdot \mathbf{r} - i\omega_2(t - \tau)) + \text{c.c.} \quad (1)$$

Here $\mathbf{k}_j$, ω_j, $\mathbf{e}_j$, and $\mathcal{E}_j$ are the wavevector, carrier frequency, polarization vector, and complex envelope of the jth pulse, respectively. The system is excited by a pump pulse and the transmission of the probe pulse is recorded after a delay τ (see Fig. 1).[4,52,53]
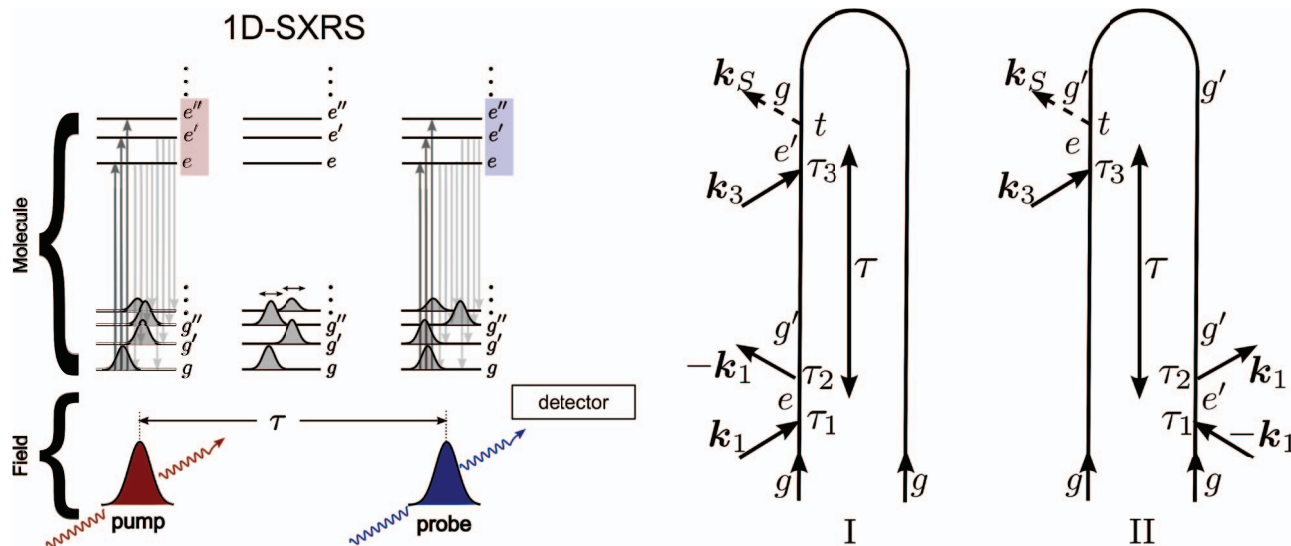

FIG. 1. Loop diagrams, pulse sequence, and core and valence energy levels for the 1D-SXRS signal.

Each pulse interacts with the system twice via a stimulated Raman process. A core-electron is excited into an unoccupied orbital during each pulse; the excited system then evolves for a short period before a second interaction with the same pulse stimulates a valence electron to destroy the core-hole, emitting an x-ray photon in the process. The system is left in a coherent superposition of valence excited states after interaction with the first x-ray pulse which interferes with the amplitude of the Raman process with the second pulse, leading to a change in its transmitted intensity.[42] The 1D-SXRS signal is defined as the change in the transmission of the second pulse with or without the pump pulse, as a function of the delay between the two pulses. We neglect nuclear motions, further work will be needed to examine their effect on SXRS.

We consider stimulated resonance Raman excitation at soft x-ray wavelengths, which are much longer than the spatial extent of the resonant core orbitals. A phase dependent on the distance between resonant cores will not enter into the response, as each field interacts twice, canceling the phase factor of $\exp(\pm i\mathbf{k}_j \cdot \mathbf{R}_n)$. Taking the delay between pulses

(τ) to be long compared with the lifetime for core-excited states (<10 fs for nitrogen and oxygen),[54] the signal will be dominated by the ground-state bleach (GSB) contributions to the time-integrated pump-probe signal (defined as the pump-induced change in the absorption of the probe).

The closed-time path loop diagrams for the two interfering contributions to the signal are shown in Fig 1. These diagrams are similar to the double-sided ladder diagrams traditionally used to describe nonlinear optical spectroscopy,[5] with a few key differences. We read the loop diagram by starting with the ground state on the lower left corner and moving upwards, describing forward evolution (propagation of the ket). Interactions with the field are represented by arrows facing into (absorption of a photon) and out of (emission of a photon) the diagram. At the top of the loop we switch to backward time evolution (propagation of the bra), and finally arrive back at the ground state. Thus we are able to work in Hilbert space, rather than the higher dimensional Liouville space required with the density matrix (for diagram rules see Refs. 55 and 56). From Fig. 1 we get

$$\mathbb{S}_{SXRS}(\tau) = -\sum_{e,e',g'} V_{ge'} V_{e'g'} V_{g'e} V_{eg} \int_{-\infty}^{\infty} dt \int_{-\infty}^{t} d\tau_3 \int_{-\infty}^{\infty} d\tau_2 \int_{-\infty}^{\tau_2} d\tau_1 \mathcal{E}_2^*(t-\tau)\mathcal{E}_2(\tau_3-\tau)e^{-i\omega_2(\tau_3-t)}$$

$$\times [\mathcal{E}_1^*(\tau_2)\mathcal{E}_1(\tau_1)\exp(-i\omega_{e'g}t + i\omega_{e'g'}\tau_3 - i\omega_{eg'}\tau_2 + i\omega_{eg}\tau_1 - i\omega_1(\tau_1-\tau_2))$$

$$+ \mathcal{E}_1(\tau_2)\mathcal{E}_1^*(\tau_1)\exp(-i\omega_{eg'}t + i\omega_{eg}\tau_3 + i\omega_{e'g'}\tau_2 - i\omega_{e'g}\tau_1 + i\omega_1(\tau_1-\tau_2))] + \text{c.c.} \tag{2}$$

Here $|g\rangle$ is the electronic ground state, $|e\rangle$ is a state with a core-hole, and $|g'\rangle$ is a valence excited state (see Fig. 1). Equation (2) can be recast as

$$\mathbb{S}_{SXRS}(\tau) = \Re[\langle\alpha_2(\tau)\alpha_1(0)\rangle - \langle\alpha_1^\dagger(0)\alpha_2(\tau)\rangle], \tag{3}$$

where

$$\alpha_{j;g'g''} \equiv -i\sum_e (\boldsymbol{e}_j \cdot \boldsymbol{V}_{g'e})(\boldsymbol{e}_j \cdot \boldsymbol{V}_{eg''}) \int_{-\infty}^{\infty} d\tau_2$$

$$\times \int_{-\infty}^{\tau_2} d\tau_1 \mathcal{E}_j^*(\tau_2)\mathcal{E}_j(\tau_1) \exp\left(i\Delta_{eg'}^j \tau_2 - i\Delta_{eg''}^j \tau_1\right) \tag{4}$$

is the effective polarizability weighted by the two-photon spectral density of the jth ultrashort pulse. Here $\Delta_{ev}^j \equiv \omega_j - \omega_{ev} + i\Gamma_e$ is the detuning for the $v \to e$ transition, and Γ_e is the inverse of the core-hole lifetime. In Eq. (4) we have included the direction cosines between the pulse polarization vector and the transition dipoles, as well as the core-excited lifetime Γ_e. Equation (4) can be recast in the frequency domain as

$$\alpha_{j;g'g''} = \sum_e \frac{(\boldsymbol{e}_j \cdot \boldsymbol{V}_{g'e})(\boldsymbol{e}_j \cdot \boldsymbol{V}_{eg''})}{2\pi}$$

$$\times \int_{-\infty}^{\infty} d\omega_2 \frac{\mathcal{E}_j^*(\omega_2)\mathcal{E}_j(\omega_2 + \omega_{g'g''})}{\omega_2 + \Delta_{eg'}^j}. \tag{5}$$

The first term in Eq. (3) (diagram I from Fig. 1) can be viewed as a valence wavepacket $\alpha_1|\psi_0\rangle$, created by pulse 1, which propagates forward in time τ and overlaps with a window wavepacket $\langle\psi_0|\alpha_2$ created by pulse 2. The second term (diagram II) can be viewed as a window wavepacket created by pulse 2 $\alpha_2|\psi_0\rangle$ propagating backwards in time $-\tau$ to overlap with the doorway $\langle\psi_0|\alpha_1$ created by pulse 1.

Hereafter we assume linearly polarized Gaussian pulses, with the spectral envelope function

$$\mathcal{E}_j(\omega) = \sqrt{2\pi}\sigma_j e^{-\sigma_j^2\omega^2/2 - i\phi_j}, \tag{6}$$

where σ_j is the temporal pulse width (equal to intensity FWHM divided by $2\sqrt{\ln 2}$). The absolute phase ϕ_j of the jth pulse does not affect the signals considered here. Inserting

Eq. (6) in Eq. (5), the effective polarizability becomes

$$\alpha_{j;g'g''} = -\frac{1}{2}\sum_e (\boldsymbol{e}_j \cdot \boldsymbol{V}_{g'e})(\boldsymbol{e}_j \cdot \boldsymbol{V}_{eg''})\mathcal{E}_j^*\left(\Delta_{eg'}^j\right)\mathcal{E}_j\left(\Delta_{eg''}^j\right)$$

$$\times\left[i + \text{erfi}\left(-\sigma_j(\Delta_{eg'}^j + \Delta_{eg''}^j)/2\right)\right], \quad (7)$$

where

$$\text{erfi}(x) = -\frac{2i}{\sqrt{\pi}}\int_0^{ix} dt\, e^{-t^2} \quad (8)$$

is the imaginary error function (see Appendix A for details). The treatment so far (Eqs. (4), (5), and (7)) has assumed the molecule is oriented in the lab frame. Of course, under typical experimental conditions in the gas or condensed phases, the material will be an ensemble of randomly oriented molecules. All signals presented below are orientationally averaged, assuming all incoming fields are polarized parallel to each other, using the framework of Ref. 57. The necessary tensor expressions for the 2D-SXRS signal are given in Appendix B.

The form for the effective polarizability given in Eq. (5) is general, and can easily be extended to cover the possibility that the upward and downward transitions are facilitated by different pulses whose arrival times coincide. The theoretical formalism presented is also well suited explore the use of pulse shaping[58–61] to optimize the Raman signals and highlight desired features. The experimental difficulties for x-ray pulse-shaping are daunting, but technological progress in this area is proceeding very rapidly.

The operator α_j is complex and symmetric and therefore non-Hermitian.[62] We define its Hermitian and anti-Hermitian components as

$$\alpha_j^H = (\alpha_j + \alpha_j^\dagger)/2,$$
$$\alpha_j^{AH} = (\alpha_j - \alpha_j^\dagger)/2. \quad (9)$$

The matrix elements of these operators are easily found from Eq. (7),

$$\alpha_{j;g'g''}^H = -\frac{1}{2}\sum_e (\boldsymbol{e}_j \cdot \boldsymbol{V}_{g'e})(\boldsymbol{e}_j \cdot \boldsymbol{V}_{eg''})\mathcal{E}_j^*\left(\Delta_{eg'}^j\right)\mathcal{E}_j\left(\Delta_{eg''}^j\right)$$
$$\times \text{erfi}\left(-\sigma_j(\Delta_{eg'}^j + \Delta_{eg''}^j)/2\right),$$

$$\alpha_{j;g'g''}^{AH} = -\frac{i}{2}\sum_e (\boldsymbol{e}_j \cdot \boldsymbol{V}_{g'e})(\boldsymbol{e}_j \cdot \boldsymbol{V}_{eg''})\mathcal{E}_j^*\left(\Delta_{eg'}^j\right)\mathcal{E}_j\left(\Delta_{eg''}^j\right). \quad (10)$$

The 1D-SXRS from Eq. (3) may be rewritten as

$$\mathbb{S}_{SXRS}(\tau) = 2\Re\langle\alpha_2^{AH}(\tau)\alpha_1(0)\rangle. \quad (11)$$

This signal depends on only on the anti-Hermitian part of the polarizability for the probe pulse, which, as Eq. (10) shows, decreases more rapidly with off-resonant detuning. We may ignore vibrational contributions to the elastic component of the signal which depends on $\alpha_{1;gg}$. The short core-excited state lifetime precludes a vibrational phase evolving on this potential energy surface; the x-ray polarizability is diagonal in the vibrational subspace within the Condon approximation.

Vibrational progressions may appear for long delays as an additional fine structure to the 1D and 2D signals. These are not included in the present simulations.

III. TWO DIMENSIONAL STIMULATED RAMAN: 2D-SXRS

In 2D-SXRS the transmitted intensity of the third pulse depends on two pulse delays. The 2D signal is related to $\chi^{(5)}$, whereas the 1D-SXRS pump-probe signal is associated with $\chi^{(3)}$.[17] The extra time-delay period allows more complicated valence electronic dynamics to be prepared and probed. Again we assume that the delay times t_1 and t_2 are long compared to the core-hole lifetime, any core-excited populations created by the pulses may be safely neglected. The 2D-Raman signal is represented by the four diagrams in Fig. 2. Using a single-particle picture, the first pulse creates an electron-hole pair in either the ket (diagrams i and iv) or the bra (diagrams ii and iii). The second pulse can either create another electron-hole pair (as in diagrams i and iii), or change the electron-hole pair created by the first (diagrams ii and iv). In either case the pairs created by the first and the second pulses must share either a common hole or electron in order to survive the trace. These diagrams represent different sequences of forward and/or backward time evolution of valence wavepackets. These generalize Fig. 1 which has a single evolution period. The expression for the Raman signal can be read directly from the diagrams in Fig. 2 and is given by

$$\mathbb{S}_{2D-SXRS}(t_1, t_2) = \Im\left[\mathbb{S}_i + \mathbb{S}_{ii} + \mathbb{S}_{iii} + \mathbb{S}_{iv}\right], \quad (12)$$

where

$$\mathbb{S}_i = -\langle\alpha_2^\dagger(t_1)\alpha_3(t_2 + t_1)\alpha_1(0)\rangle,$$
$$\mathbb{S}_{ii} = \langle\alpha_1^\dagger(0)\alpha_2^\dagger(t_1)\alpha_3(t_2 + t_1)\rangle,$$
$$\mathbb{S}_{iii} = -\langle\alpha_1^\dagger(0)\alpha_3(t_2 + t_1)\alpha_2(t_1)\rangle, \quad (13)$$
$$\mathbb{S}_{iv} = \langle\alpha_3(t_2 + t_1)\alpha_2(t_1)\alpha_1(0)\rangle.$$

This signal may also be recast as

$$\mathbb{S}_{2D-SXRS}(t_1, t_2) = 2\Im\left[\langle\alpha_3^{AH}(t_1 + t_2)\alpha_2(t_1)\alpha_1(0)\rangle - \langle\alpha_1(0)\alpha_3^{AH}(t_1 + t_2)\alpha_2^\dagger(t_1)\rangle\right]. \quad (14)$$

The first term in Eq. (14), $\mathbb{S}_{ii} + \mathbb{S}_{iv}$, is the time-dependent overlap, within a resonance window determined by the probe pulse, between the ground state and a valence wavepacket that has interacted with both pump pulses. The second term, $\mathbb{S}_i + \mathbb{S}_{iii}$, is the overlap between different Raman wavepackets.

IV. SIMULATIONS FOR THE OXYGEN AND NITROGEN K-EDGES OF NMA

A. Electronic structure calculations

The trans-NMA core-excited states are modelled as single core-hole/virtual orbital electron pairs in the static exchange (STEX) molecular orbital (MO) basis using the
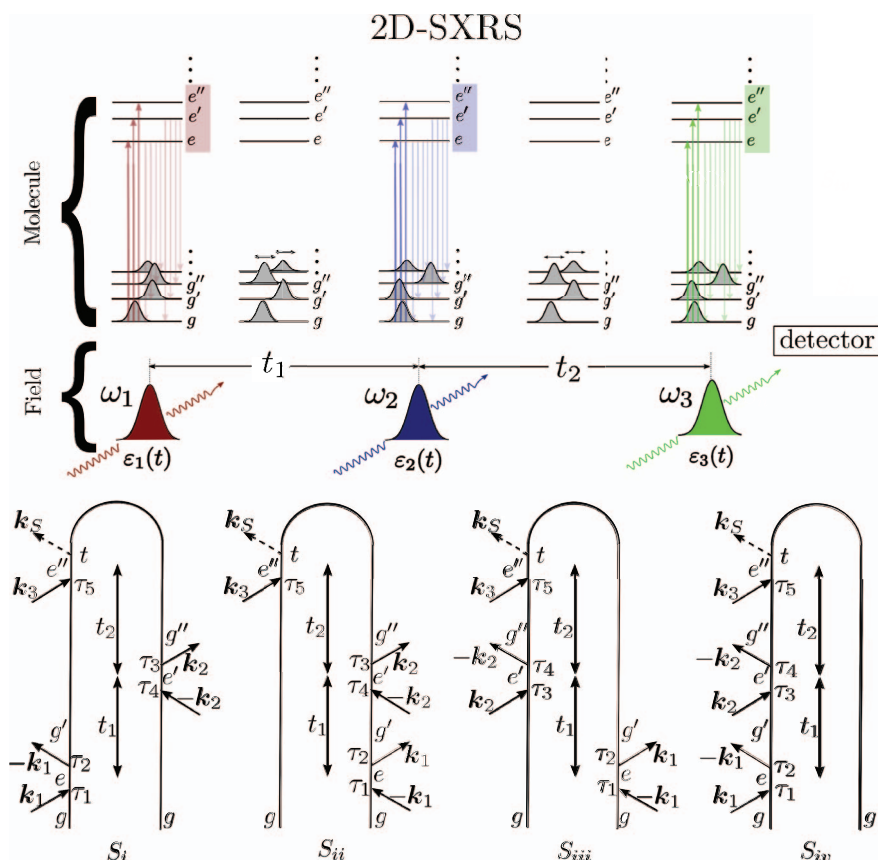
FIG. 2. Loop diagrams, pulse sequence, and energy levels for the 2D-SXRS signal.

orbital approximation. Valence excited states are treated at the configuration interaction singles (CIS) level of theory. Both in STEX and CIS Hartree-Fock (HF) orbitals are employed. In order to keep the level of theory consistent we have calculated the excited states using CIS, which is known to overestimate the adiabatic excitation energies.[63] More accurate TDDFT methods to calculate the core excitation energies are under development.[64] The geometry of *trans*-NMA was optimized using the quantum chemistry package GAUSSIAN 09 (Ref. [65]) at the B3LYP/6-311G** level. The STEX model,[66–68] in which a core-ionized Fock matrix is constructed which includes the core-hole self-consistently, was implemented in a modified version of the quantum chemistry package PSI3,[69] with an implementation described in Appendix C of Ref. [53]. All transition frequencies and dipole moments for core-excited states were calculated using the orbital approximation at the HF/6-311G** level. Fig. 3 shows the largest amplitude natural transition orbitals[70] between the ground and excited states which contribute to Figs. 9–13, obtained by a singular value decomposition of the CIS transition densities.

Using Fermi creation and annihilation operators for the valence (c) and core (d) molecular orbitals, the core-excited states are given by

$$|e\rangle = |jn\rangle = c_j^\dagger d_n |e_o\rangle, \qquad (15)$$

where $|e_o\rangle$ is the lowest energy core excited state. The valence excited states are

$$|g'\rangle = \sum_{ai} C_{ai}^{g'} |ai\rangle = \sum_{ai} C_{ai}^{g'} c_a^\dagger c_i |g\rangle, \qquad (16)$$

where $C_{ai}^{g'}$ are the CI coefficients for state $|g'\rangle$.

B. Valence excitations and UV absorption

Earlier simulations on trans-NMA presented in Ref. [53] approximated the valence excited states as single electron-hole pairs in the HF MO basis. The lowest energy valence-excited state then involved a transition from the highest occupied orbital to the lowest virtual orbital, a HOMO to LUMO transition. The excitation energy was approximated as the difference in MO energies, which gave 14.35 eV. Here we use a higher level treatment of valence excited states obtained by diagonalizing the singly excited block of the Hamiltonian. The lowest-energy excitation is now found to be 6.92 eV (see Table I for a list of the CIS energies), which is consistent with experimental vacuum-UV absorption results from trans-NMA.[71] The valence excitations and the Raman peaks presented here (between 7 and 18 eV) are very different from those in Ref. [53].

The calculated UV absorption spectrum is displayed in Fig. 4. The molecule is taken to be initially in the ground state
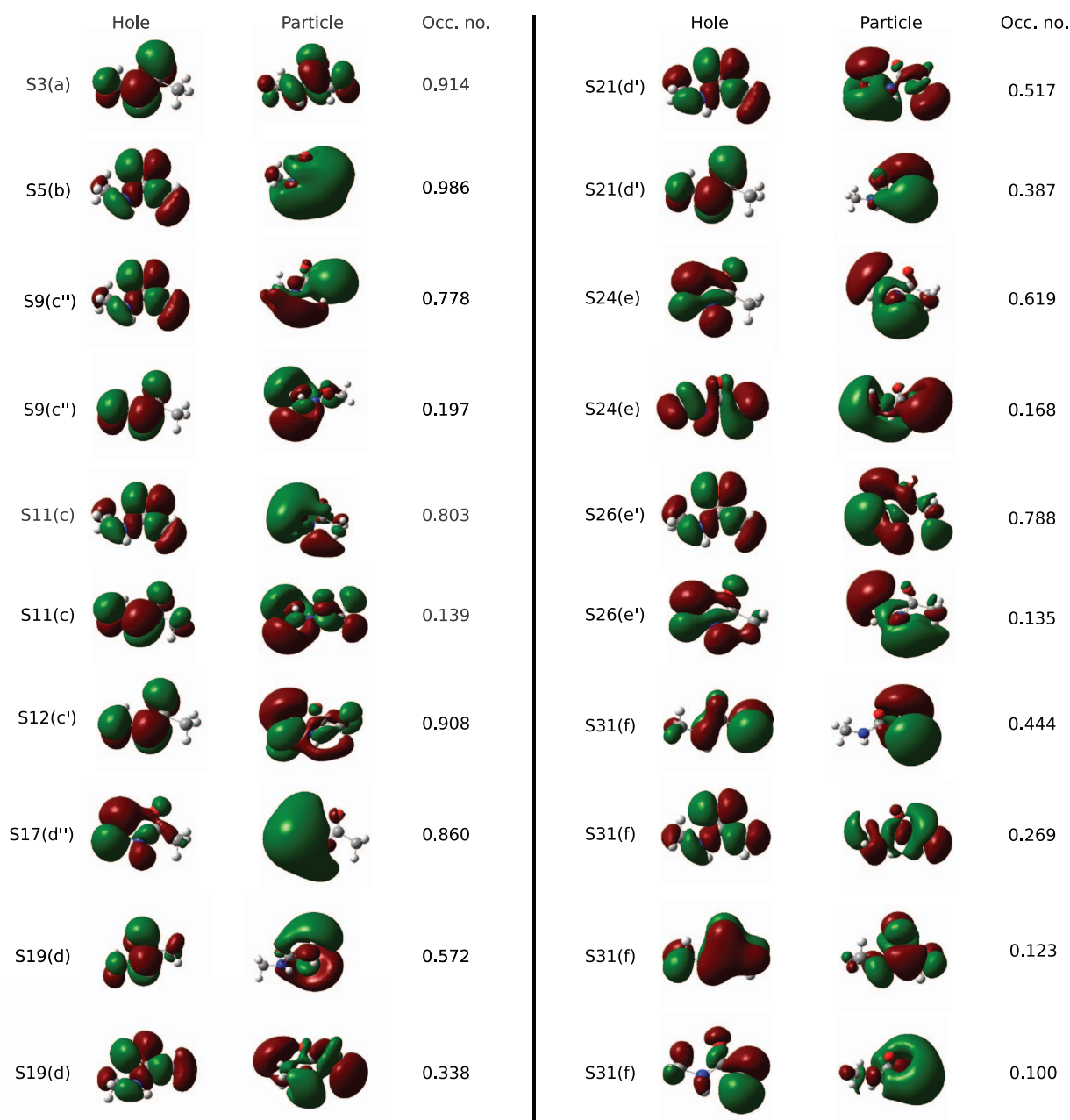
	Hole	Particle	Occ. no.		Hole	Particle	Occ. no.
S3(a)			0.914	S21(d')			0.517
S5(b)			0.986	S21(d')			0.387
S9(c'')			0.778	S24(e)			0.619
S9(c'')			0.197	S24(e)			0.168
S11(c)			0.803	S26(e')			0.788
S11(c)			0.139	S26(e')			0.135
S12(c')			0.908	S31(f)			0.444
S17(d'')			0.860	S31(f)			0.269
S19(d)			0.572	S31(f)			0.123
S19(d)			0.338	S31(f)			0.100

FIG. 3. Natural transition orbitals of the dominant excitations in Figs. 11–13.

and the $\delta(\omega - \omega_{g'g})$ in Fermi's golden rule was replaced by a Lorentzian, with an effective lifetime $\Gamma_{g'}$, to account for the linewidth of valence electronic transitions

$$\mathbb{S}_{UV}(\omega) = \sum_{g'} \frac{|\mu_{g'g}|^2 \Gamma_{g'}}{(\omega - \omega_{g'g})^2 + \Gamma_{g'}^2}. \quad (17)$$

An accurate estimate of $\Gamma_{g'}$ would require potential energy surface calculations and characterization of any conical intersections or dissociative states which could cause decay of the excited state population in $|g'\rangle$. We set $\Gamma_{g'} = 0.05$ eV for all valence excitations in all simulations for display purposes.

C. Frequency domain XANES and RIXS spectra

In Fig. 5 we present the x-ray absorption near-edge structure (XANES) spectra calculated for an isotropic trans-NMA sample, excited at the nitrogen and oxygen K-edges. The XANES and the UV absorption spectra were calculated using a Lorentzian lineshape to account for core lifetime broadening and pure dephasing

$$\mathbb{S}_{XANES}(\omega) = \sum_{e} \frac{|\mu_{eg}|^2 \Gamma_e}{(\omega - \omega_{eg})^2 + \Gamma_e^2}. \quad (18)$$

As in Ref. 53, we set the first XANES transition for nitrogen to 401.7 eV and to 532.0 eV for oxygen, to match experiment.[72] Each XANES peak represents an excitation

TABLE I. CIS valence excited state energies $\{\omega_{g'g}\}$.

State	Energy (eV)	State	Energy (eV)
S_1	6.92	S_{26}	13.64
S_2	8.14	S_{27}	13.80
S_3	8.95	S_{28}	13.95
S_4	9.99	S_{29}	14.04
S_5	10.23	S_{30}	14.14
S_6	10.92	S_{31}	14.25
S_7	11.32	S_{32}	14.27
S_8	11.35	S_{33}	14.32
S_9	11.41	S_{34}	14.59
S_{10}	11.66	S_{35}	14.59
S_{11}	11.78	S_{36}	14.85
S_{12}	11.83	S_{37}	14.89
S_{13}	11.86	S_{38}	14.91
S_{14}	12.11	S_{39}	14.91
S_{15}	12.30	S_{40}	15.09
S_{16}	12.35	S_{41}	15.10
S_{17}	12.54	S_{42}	15.22
S_{18}	12.64	S_{43}	15.25
S_{19}	12.68	S_{44}	15.39
S_{20}	12.71	S_{45}	15.50
S_{21}	12.84	S_{46}	15.59
S_{22}	13.01	S_{47}	15.63
S_{23}	13.44	S_{48}	15.69
S_{24}	13.49	S_{49}	15.81
S_{25}	13.55	S_{50}	15.92

FIG. 5. Simulated XANES from trans-NMA at the nitrogen (top) and oxygen (bottom) K-edge. The stick spectra (black lines) have been convoluted with a lineshape function (see text) to give the spectra in red. Shown in blue are the power spectra for the Gaussian pulses used in the time-domain experiments described here.

from the core orbital to a bound virtual orbital. Orbitals with energies above the ionization potential are coupled to a continuum of photoelectron states. The linewidth for nitrogen was taken as: $\Gamma_{eN} = 0.4$ eV for energies up to 408 eV, and ramped up to 1.5 eV at 415 eV and held constant for higher energies. A similar form was followed for oxygen: $\Gamma_{eO} = 0.4$ eV for energies up to 537 eV, and ramped up to 1.5 eV at 544 eV and held constant thereafter. These phenomenological linewidths, which were used in earlier studies to match experimental XANES spectra of small nitrogen and oxygen containing organic molecules,[52,73] can reflect a variety of broadening mechanisms, including vibrational motion of the
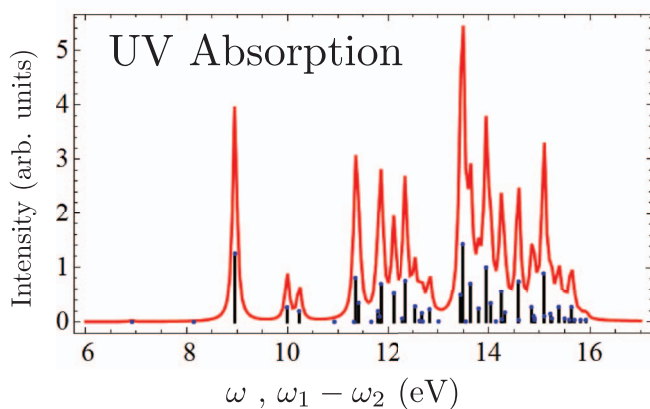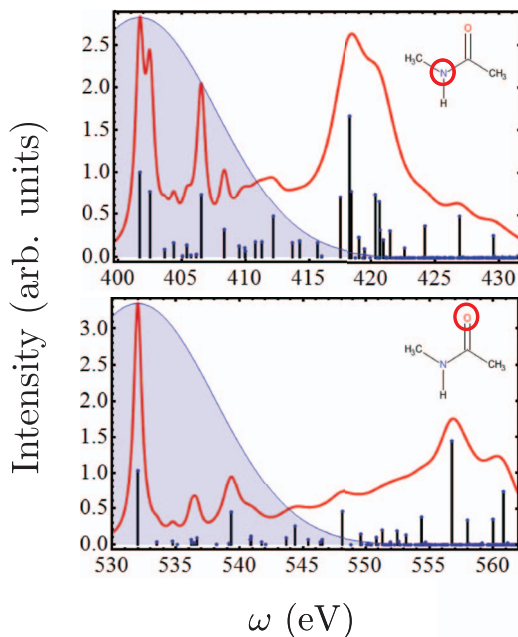
core-ionized molecule, autoionization of the excited electron and direct photoionization of the core into a photoelectron state. An exact treatment of these effects would require a Wigner-Weisskopf treatment of the decay of the bound excited electron into a continuum of photoelectron states, and potential energy surface calculations of these core-excited states. We use the atomic core-lifetime given in Sec. II in the calculation of α.

To set the stage we first calculate the traditional frequency-domain spontaneous Raman (RIXS) spectra. These should serve as a reference for comparing with the 1D-SXRS signals. The optical resonant Raman technique probes which vibrational modes of a molecule are perturbed by a given electronic excitation. Only those modes whose potential is different in the ground and excited electronic states have Franck-Condon activity. In RIXS a core electron is excited into an empty virtual orbital and then de-excited. Inelastic losses representing valence excitations can be created directly, when an electron other than the excited core electron drops into the core-hole, or indirectly when the Coulomb potential of the transiently created core-hole creates valence excitations.[74,75] The energy satellite spectra for the indirect process represent valence shake-up states and are dependent on the excitation frequency.

In RIXS a monochromatic x-ray beam (ω_1) impinges on the molecule, and the scattered radiation (ω_2) is frequency resolved, with peaks recorded vs. $\omega_1 - \omega_2 = \omega_{g'g}$. Here we take the incident beam ω_1 to be polarized, and the scattered light ω_2 is also sent through a polarization filter before detection (detected parallel to the excitation polarization). The Kramers-Heisenberg formula with a Lorentzian, linewidth
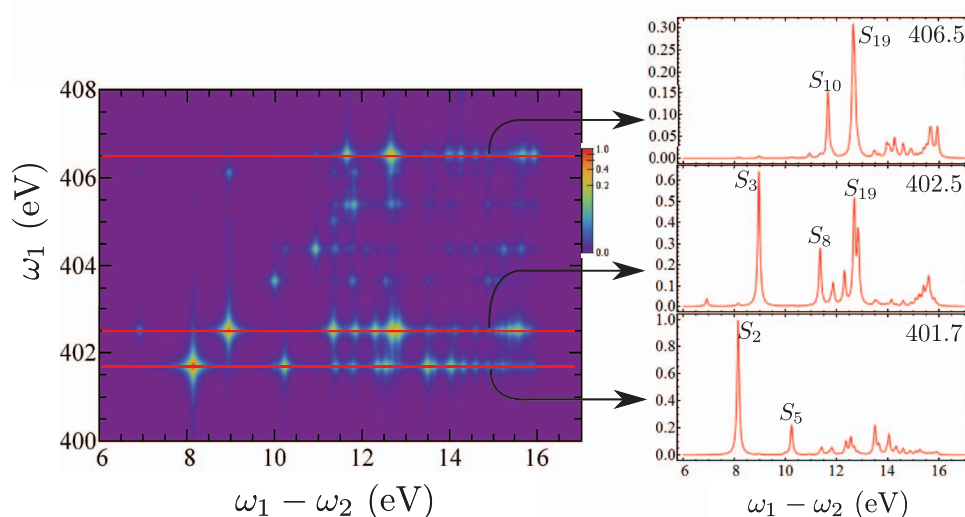

FIG. 4. Calculated UV-absorption spectrum of NMA.

FIG. 6. Calculated RIXS signal at the nitrogen K-edge from trans-NMA.

$\Gamma_{g'} = 0.05$ eV, gives

$$\mathbb{S}_{RIXS}(\omega_1, \omega_2) = \sum_{g'} \frac{|\tilde{\alpha}_{g'g}(\omega_1)|^2 \Gamma_{g'}}{(\omega_1 - \omega_2 - \omega_{g'g})^2 + \Gamma_{g'}^2}, \quad (19)$$

where

$$\tilde{\alpha}_{g'g}(\omega_1) = \sum_e \frac{(\mathbf{e}_I \cdot \mu_{g'e})(\mathbf{e}_I \cdot \mu_{eg})}{\omega_1 - \omega_{eg} + i\Gamma_e} \quad (20)$$

is the frequency-dependent resonant polarizability. Equation (20) applies to an oriented molecule in the lab frame. To account for the isotropic distribution of molecules, we orientationally averaged Eqs. (19) and (20) assuming parallel excitation and detection polarization.[76]

The calculated RIXS spectra with the incident light tuned to the nitrogen and oxygen K-edge are displayed in Figs. 6 and 7, respectively. The RIXS intensity falls off as the laser frequency is detuned from the strong core-edge transition, as expected from Eq. (20). The peak pattern changes with ω_1, since the intensity also depends on the transition dipole between the valence-excited state in question and the core-excited state in resonance with the laser frequency.

When $\omega_1 = 401.7$ eV, the transition frequency for the first N1s core-excited state, the valence-excited states S_2 and S_5 are strongly Raman active. Tuning ω_1 to be resonant with the second core-excited state causes these peaks to be replaced by a strong S_3 peak. Changing the excitation frequency to 406.5 eV (the ninth core-excited state) we see the absence of S_2, S_3, and S_5 peaks, and the dominant peak is now from the S_{19} state. The oxygen RIXS spectrum, shown in Fig. 7, shows a similar pattern. The signal is strong at the core edge, $\omega_1 = 532.0$ eV, and is dominated by the S_3, S_{15}, and S_{19} peaks. Increasing the excitation frequency to 536.6 eV gives strong peaks for S_{11} and S_{27}. This atomic selectivity makes RIXS a powerful tool for probing the delocalization of valence excited states.[77,78]

While the valence-excited states that contribute to the UV absorption spectrum and the RIXS and SXRS spectra are the same, their intensities are radically different, as can be seen by comparing Fig. 4 with Figs. 6 and 7. This is because the absorption is determined by the dipole moment between the HF ground state and the valence-excited state, while the Raman spectra depend on the polarizability resonant with a given core-excited state.
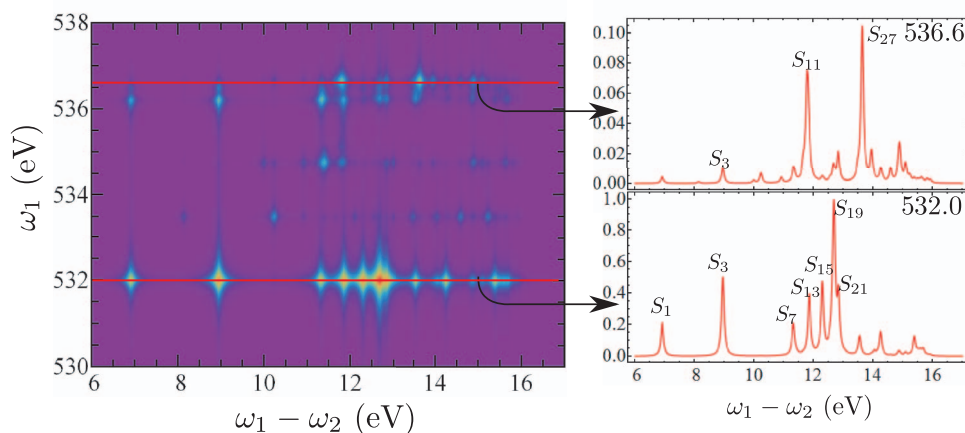

FIG. 7. Calculated RIXS signal from trans-NMA at the oxygen K-edge.

D. Time-domain stimulated X-ray Raman spectroscopy: 1D-SXRS

In both 1D-SXRS and RIXS,[79] information on valence excited states is obtained through transient excitation of core excited states. 1D-SXRS has two advantages over its frequency domain counterpart. First, because the interaction times are constrained by the field pulse envelopes, it should be possible to probe electronic dynamics directly by preceding the two Raman pulses with an initiation pulse. This pulse could prepare the molecule in some nonstationary state which may then be probed by an SXRS experiment, in much the same way as is currently done in vibrational spectroscopy.[80] We do not pursue this course here, rather we look at another advantage inherent in the time-domain experiment. We can use a two color scheme, where the two pulses are tuned to be resonant with different core transitions, providing an additional experimental knob to turn. The differences between SXRS spectra with different pulse configurations could help shed light on the nature of the valence excited states of a molecule. The two diagrams in Fig. 1 recast the SXRS spectrum as a two-slit experiment where valence wavepackets created on either the ket or the bra by the first pulse are probed by another wavepacket created in the ket by the second pulse.

The calculated 1D-SXRS signal is displayed as the Fourier transform of Eq. (3),

$$\mathbb{S}_{SXRS}(\Omega)$$

$$= \int_0^\infty d\tau \, \mathbb{S}_{SXRS}(\tau) \exp[i\Omega\tau]$$

$$= -\sum_{g'} \frac{\Re(\alpha_{2;gg'}\alpha_{1;g'g})(\Gamma_{g'} - i\Omega) + \Im(\alpha_{2;gg'}\alpha_{1;g'g})\omega_{g'g}}{(\Gamma_{g'}^2 - 2i\Gamma_{g'}\Omega - \Omega^2 + \omega_{g'g}^2)}$$

$$+ \frac{\Re((\alpha_{1;gg'})^*\alpha_{2;g'g})(\Gamma_{g'} - i\Omega) + \Im((\alpha_{1;gg'})^*\alpha_{2;g'g})\omega_{gg'}}{(\Gamma_{g'}^2 - 2i\Gamma_{g'}\Omega - \Omega^2 + \omega_{g'g}^2)}.$$

$$\tag{21}$$

Unlike RIXS (Eq. (19)), $\mathbb{S}_{SXRS}(\Omega)$ results from the interference of the two pathways in Fig. 1 and may not be written as an amplitude squared. The signal is collected in the time domain, and Fourier transformed numerically. It is important that the interpulse delay be longer than the core-hole lifetime (>10 fs). In this case, any interaction with the pulses that results in a core-excited population will decay to an ionized state through an Auger process, with transitions that are detuned from the resonant excitation with the probing pulse. If the core-hole lifetimes were long compared to the delay, the signal would be distorted by an interference between the wavepacket produced on the core-excited states and the ground valence electronic wavepacket.[52] We also neglect a τ-independent contribution to the signal, resulting from elastic scattering with $g' = g$. This can be removed experimentally.

The Hermitian and anti-Hermitian parts of the resonant polarizability matrix α averaged over the pulse bandwidth are shown in Fig. 8. We assume pulses with Gaussian envelopes, durations of $\sigma_j = 77$ as ($1/\sigma_j \approx 8.5$ eV), and center frequencies set to the N and O K-edge transitions (401.7 eV and 532.0 eV, respectively). The axes are labeled
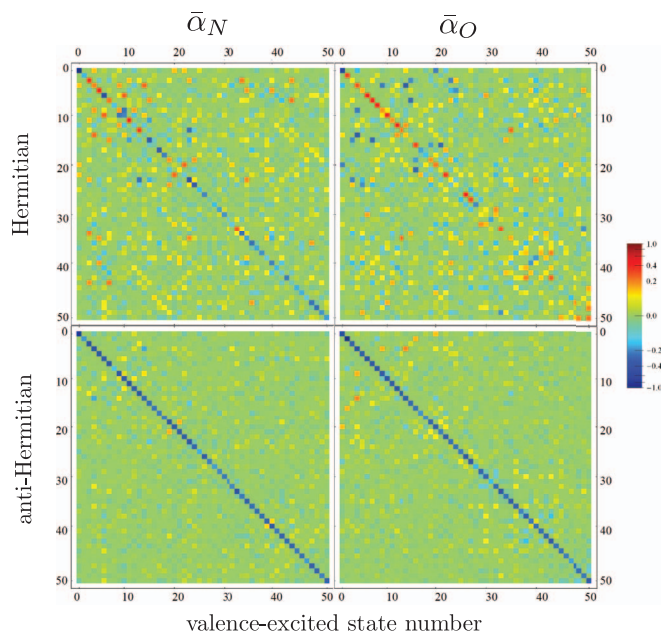

FIG. 8. Hermitian and anti-Hermitian parts of the effective isotropic polarizabilities (Eq. (7)) for the two pulses used in our simulations corresponding to the nitrogen and oxygen K-edge excitations, plotted using an arcsinh nonlinear scale (shown on the right). The Hermitian part is purely real, while the anti-Hermitian part is purely imaginary. The axes are labeled by the state numbers, 0 for the ground state, 1 for S_1, etc. State assignments can be found in Table I.

by the valence excited state number, with 0 referring to the ground state. We display the isotropic polarizability $\bar{\alpha}_j$, obtained by replacing the direction cosine term $(e_j \cdot V_{g'e})(e_j \cdot V_{eg''})$ with $V_{g'e} \cdot V_{eg''}$ in Eq. (4). Otherwise, it would be necessary to adopt a given molecular lab-frame orientation to visualize α_j. This 1D SXRS spectrum probes matrix elements of the effective polarizability in Eq. (7) between the ground state and the set of singly excited state, $\alpha_{j;gg'}$ for $j = $ N, O. The 1D-SXRS signal is a function of the top row of this symmetric matrix.

The simulated 1D-SXRS signals are shown in Fig. 9. Parallel field polarizations are used, and the signal is averaged over an isotropic distribution of molecules.[57] The 4 rows represent the four possible pulse configurations, e.g., row 3 is labeled ON signifying that the first pulse is tuned to the oxygen and the second pulse to the nitrogen K-edge. The three columns show the real, imaginary, and modulus of Eq. (21).

The one-color, time-domain signals in the top two rows of Fig. 9 resemble their frequency-domain counterparts of Figs. 6 and 7. In the N-edge RIXS spectrum, the S_2 and S_3 peaks are strong when the excitation frequency is set to 401.7 eV and 402.5 eV, respectively. Both peaks show up prominently in the NN 1D-SXRS spectrum. Since the excitation must be broadband to coherently excite valence excited states, 1D-SXRS does not select a given e state. An interesting possibility will be to use a combination of narrow band excitation combined with broadband stimulated de-excitation, as is commonly done in optical Raman spectroscopy, to regain this selectivity over core-excited states.

Two-color 1D-SXRS signals have no RIXS analogue. In the third and fourth rows of Fig. 9 we show the ON and NO
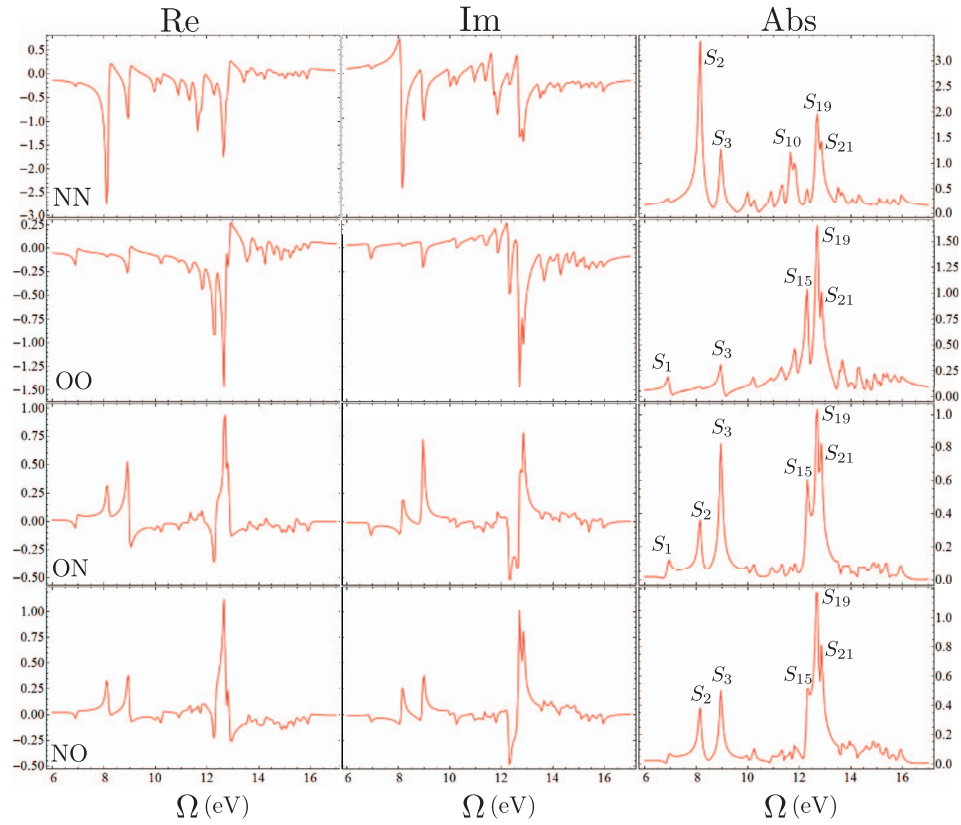
FIG. 9. Calculated SXRS spectra from trans-NMA, in which both pulses are polarized parallel to the lab frame V axis. The pulses are Gaussian, 181 as FWHM in intensity, with center frequency set to either 401.7 eV (N) or 532.0 eV (O). From left to right we show the real part, imaginary part, and modulus of Eq. (21). The two-color signals (bottom two rows) have their pulse sequences given from left to right in chronological order, i.e., the ON signal results from having the O pulse come first and the N pulse come second.

spectra. The moduli of these two signals are virtually identical but differ in their real and imaginary parts. The S_2 peak is mostly absent from the OO signal, very strong in the NN signal, and moderate in the ON and NO signals. However, the two-color signals are not simply averages of the one-color signals from the top two rows. For instance, the S_{10} peak that shows up prominently in the NN spectrum is missing completely from the two-color spectra. Thus, two-color 1D-SXRS provides a different window into the interaction between core-hole excitation and valence-excited states.

E. Two-dimensional stimulated Raman: 2D-SXRS

The 2D-SXRS signal in Eq. (13) is the product of $\alpha_{1;g'g}$ and $\alpha_{k;gg''}$, from the top row of the polarizability matrix with a third term, $\alpha_{l;g'g''}$ from its interior (see Fig. 8). The 1D-SXRS signal (Eq. (21)) only depends on the first row and column of

the polarizabilities; 2D-SXRS thus carries information about correlations between dynamics in the two time periods not available in the 1D signals.

The 2D signals will be displayed in the frequency domain

$$\mathbb{S}_{2D-SXRS}(\Omega_1, \Omega_2) = \int_0^\infty dt_1$$

$$\times \int_0^\infty dt_2 e^{i\Omega_1 t_1 + i\Omega_2 t_2} \mathbb{S}_{2D-SXRS}(t_1, t_2).$$

(22)

The contribution to the 2D signal coming from, for example, diagram $\mathbb{S}_i$ (see Eq. (13)) is given by

$$\frac{\Re((\alpha_{2;gg''})^* \alpha_{3;g''g'} \alpha_{1;g'g})(\Gamma_{g'}^2 - \omega_{g'g}\omega_{g'g''} - \Omega_1\Omega_2 - i\Gamma_{g'}(\Omega_1 + \Omega_2))}{(\omega_{g'g}^2 + (\Gamma_{g'} - i\Omega_1)^2)(\omega_{g'g''}^2 + (\Gamma_{g'} - i\Omega_2)^2)}$$

$$+ \frac{\Im((\alpha_{2;gg''})^* \alpha_{3;g''g'} \alpha_{1;g'g})(\Gamma_{g'}(\omega_{g'g} + \omega_{g'g''}) - i(\omega_{g'g''}\Omega_1 + \omega_{g'g}\Omega_2))}{(\omega_{g'g}^2 + (\Gamma_{g'} - i\Omega_1)^2)(\omega_{g'g''}^2 + (\Gamma_{g'} - i\Omega_2)^2)}$$
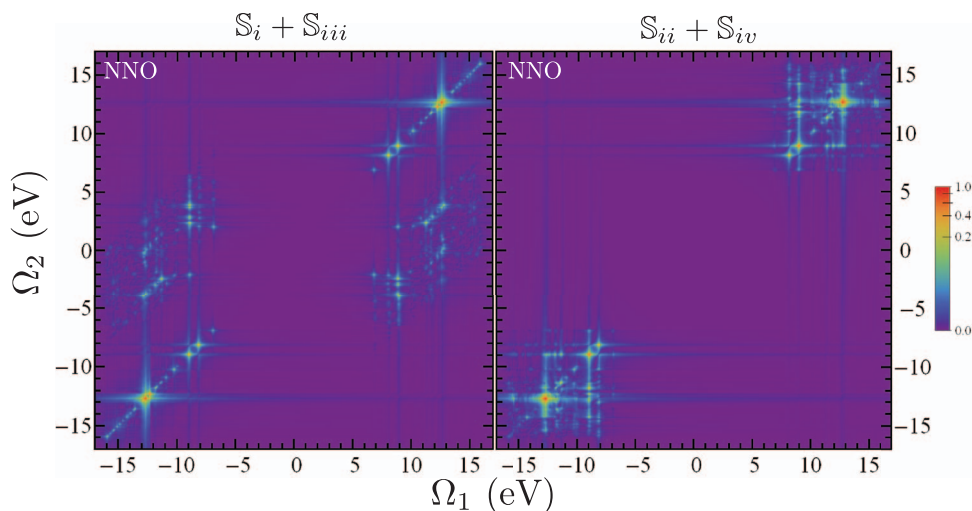
(23)

FIG. 10. Simulated 2D-XRS spectrum from trans-NMA using an NNO pulse configuration, plotted as the modulus of the Fourier transform and separated into the contributions from the two types of diagrams in Fig. 2. The labels refer to the pulse center frequency and polarization of the three pulses ordered chronologically from left to right. In the NNO signal, the first and second pulses have their center frequency resonant with the nitrogen K-edge transition, and the third pulse is likewise tuned to the oxygen K-edge. Signals are plotted using an arcsinh nonlinear scale (see color bar) to highlight weak features.

and the other contributions follow similarly. As in the 1D signal, we remove any zero frequency contributions (for Ω_1 and Ω_2) prior to plotting.

Fig. 8 shows that the anti-Hermitian part of α, for both pulses is mostly diagonal, while the Hermitian part has significant off-diagonal contributions. Since the 2D signal depends only on the anti-Hermitian part of the polarizability for the probe pulse, the probe acts as a filter through which the various valence-excited wavepackets created by the pump pulses interfere with each other.

In Fig. 10 the modulus of Eq. (22) is shown for the NNO pulse sequence, in which the first two pulses are resonant with nitrogen and the last with oxygen. Diagonal peaks are the largest features due to the large diagonal matrix elements of α^j. The contributions $\mathbb{S}_i$ and $\mathbb{S}_{iii}$ contain diagonal peaks for $g = g''$. Likewise, in $\mathbb{S}_{ii}$ and $\mathbb{S}_{iv}$, we get a diagonal peak when $g' = g''$. When different valence excited states are involved, off-diagonal peaks of two different varieties are found. $\mathbb{S}_{ii}$ and $\mathbb{S}_{iv}$ contain peaks at $(\Omega_1, \Omega_2) = (\omega_{gg'}, \omega_{gg''})$, i.e., ω_2 is a valence excitation frequency of the system. In the other diagrams, $\Omega_2 = \omega_{g'g''}$ is the difference between system excitation frequencies. Inelastic peaks from the $\mathbb{S}_i$ and $\mathbb{S}_{iii}$ contributions are therefore spectrally removed from the much stronger elastic peaks. Since each diagram contributing to the signal defined in Eq. (22) has inversion symmetry, further plots will omit the portion of the signal where $\Omega_1 < 0$.

Off-diagonal peaks are weaker than diagonal peaks because the diagonal elements of α_j are much larger than the off-diagonal elements. To enhance these features, we plot the 2D signals using the nonlinear scale,

$$\text{arcsinh}(\mathbb{S}) = \ln(\mathbb{S} + \sqrt{1 + \mathbb{S}^2}). \tag{24}$$

This scaling function interpolates between linear (for small $\mathbb{S}$) and logarithmic (for large $\mathbb{S}$) scaling and shows both weak and strong features (the modulus of the signal is taken prior to applying this scaling function).

Plots of all 8 two-color 2D-SXRS signals are given in Figs. 11 and 12. Detailed interpretation of this information, relating the intensities of the peaks in a 2D spectrum to the shape of the various orbitals and their underlying many-body wavefunctions will require further study. These signals may also prove to be a valuable test for the quality of electronic structure calculations on molecular systems.

The 1D spectra with the NO and ON pulse configurations are very similar, as may be seen in the bottom two panels of the right column of Fig. 9. However, the 2D signals, especially in the spectral region $6\,\text{eV} > \omega_2 > -6\,\text{eV}$, show a much greater sensitivity to pulse combinations. Note the radically different spectrum that results in Fig. 11 when the last two pulses are interchanged in going from the NNO to the NON configuration.

In Fig. 13 we show the OOO spectrum from Fig. 12 on an expanded scale, together with several 1D horizontal and diagonal traces. For comparison, we also show the corresponding traces from the OON signal using a blue dashed line. These two signals differ only in the frequency of the third pulse, the first and second pulses are the same. A trace along the diagonal line $\Omega_1 = \Omega_2$ is shown in panel **i** and is very similar to the OO 1D-SXRS signal, the second row, right panel from Fig. 9, with narrower linewidths. Although the S_2 peak (8.14 eV) is totally absent from the OOO signal, which is consistent with the 1D results, this peak has amplitude in the OON signal. The matrix element of α_O connecting S_0 and S_2, the square of which determines the amplitude of this peak in the OO 1D spectrum, may be small but it must be nonzero for this peak to show up in the OON signal.

A horizontal trace, with a constant $\Omega_2 = 8.95$ eV, indicating that the system is in a $|S_3\rangle\langle S_0|$ coherence during τ_2, is displayed in panel **ii**. The diagonal peak is dominant here, indicating a lack of off-diagonal peaks of the first kind,
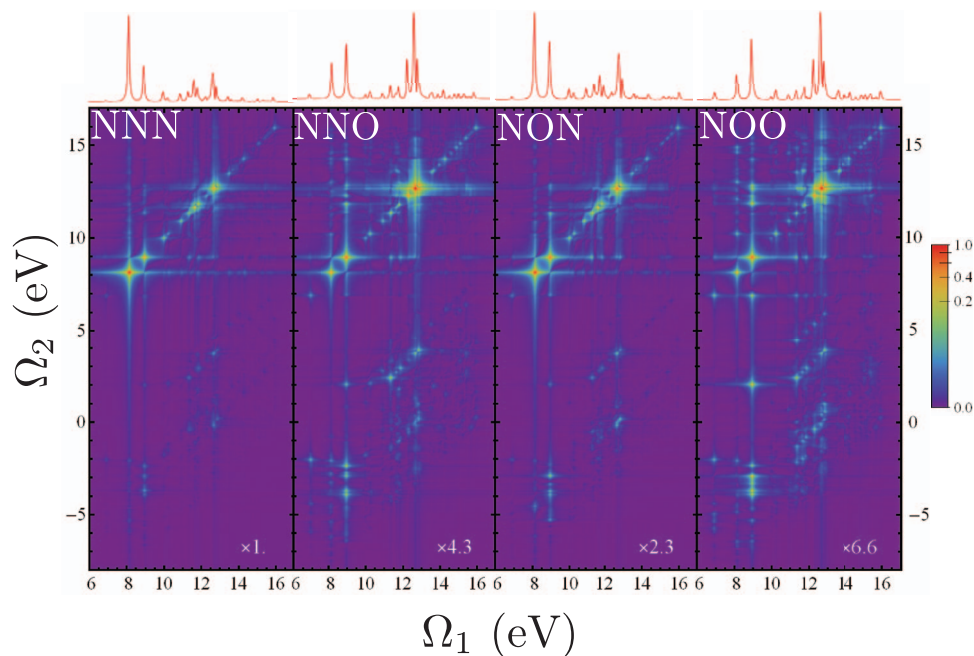
FIG. 11. Simulated 2D-XRS spectra from trans-NMA, plotted as the modulus of the Fourier transform. The labels refer to the pulse center frequency and polarization of the three pulses ordered chronologically from left to right. In the NNO signal, the first and second pulses have their center frequency resonant with the nitrogen K-edge transition, and the third pulse is likewise tuned to the oxygen K-edge. Signals are plotted using an arcsinh nonlinear scale to highlight weak features. Traces of each signal along the diagonal are shown in red on top of each signal.

those arising from diagrams $\mathbb{S}_{ii}$ and $\mathbb{S}_{iv}$. The OOO and OON signals are largely the same, with the latter being larger in magnitude. Panel **iii** shows a similar horizontal trace, with $\Omega_2 = 8.14$ eV corresponding to S_2. This trace is much larger in magnitude when the probe pulse is resonant with nitrogen core transitions, consistent with the fact that the S_2 valence state is more strongly perturbed by a nitrogen than an oxygen core-hole.

The off-diagonal peaks seen in panels **ii** and **iii** result from the interference between diagrams
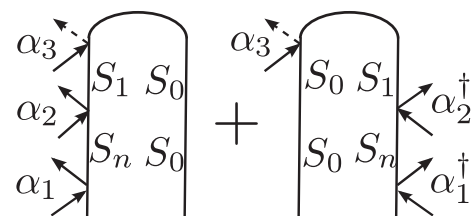
where S_n is the state giving rise to the Ω_1 frequency. The $(\Omega_1, \Omega_2) = (8.95$ eV$, 6.91$ eV$)$ peak in panel **iii**
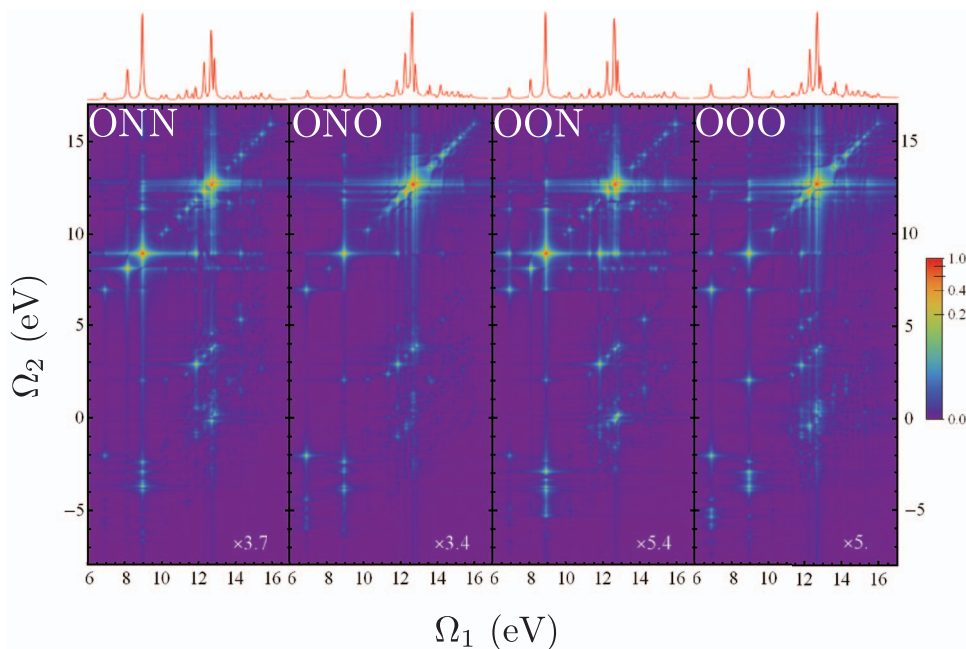

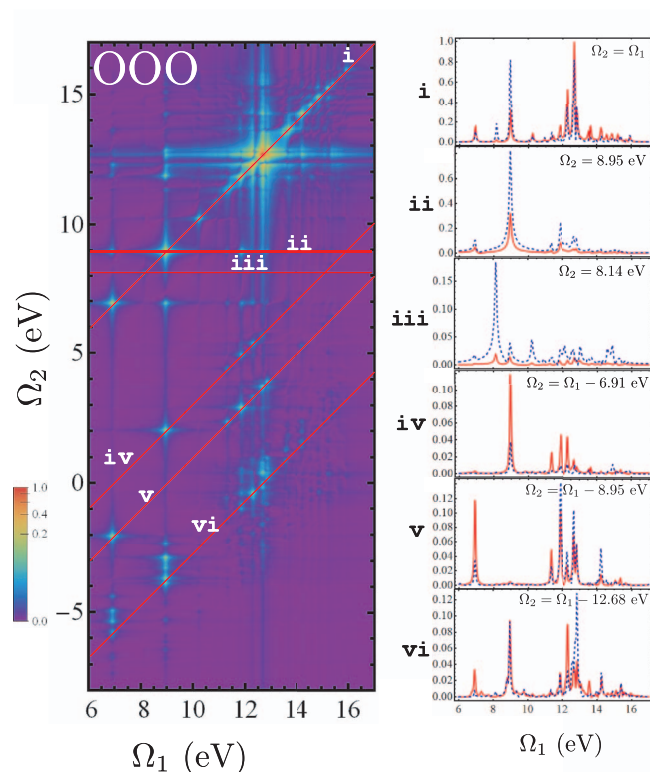FIG. 12. Same as Fig. 11 for the other pulse configurations.

FIG. 13. (Left) An enlarged version of the OOO spectrum from Fig. 11, plotted using a nonlinear scale shown on the color bar to the left. (Right) Horizontal and diagonal slices, plotted using a linear scale, of the 2D spectrum on the left (in red) plotted together with the corresponding traces from the corresponding OON (dashed, blue) to highlight the effect of changing the probe pulse in the three-pulse sequence.

depends nonlinearly on the matrix element $\alpha_{O;S_3S_1}$. Only off-diagonal peaks carry information about the polarizability *between* valence excited states. The diagonal peaks with contributions from all four diagrams in Fig. 2 are insensitive to these quantities. The diagonal peak at $(\Omega_1, \Omega_2) = (8.95\,\text{eV}, 8.95\,\text{eV})$ in panel **ii**, for example, depends on products like $\alpha_{O;S_0S_3}\alpha_{O;S_3S_3}\alpha_{O;S_3S_0}$ where the polarizability between the ground and valence excited states, which determine the linear SXRS signal, are multiplied by a diagonal element of the polarizability, seen to be much larger than off-diagonal elements in Fig. 8.

Panels **iv**, **v**, and **vi** show diagonal traces where Ω_2 is equal to the difference between two valence excitation frequencies. The peaks in panel **iv** result from interference of the following diagrams:
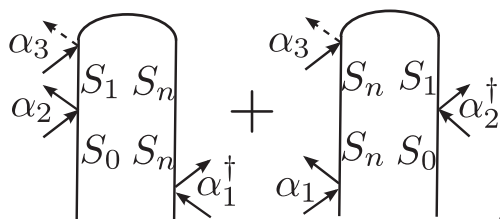
In panel **iv** the signal is much weaker with a nitrogen probe than with an oxygen probe though they are similar in shape. This is contrast with the two-color 1D results from Fig. 1,

where the S_1 peak is much stronger with a nitrogen probe than with an oxygen probe.

Panels **ii** and **v** both show signals where the second pulse leaves the system in the S_3 state, however they do so using the two different types of diagrams discussed above. The fact that these spectra are so different in appearance demonstrates the wealth of information available using 2D-SXRS.

V. CONCLUDING REMARKS

We have calculated and analyzed multidimensional stimulated x-ray Raman spectroscopy signals at the N and O K-edge. The signals are sensitive to the order in which the atom-specific x-ray excitations are used to perturb and probe the valence electron configuration. The relative intensities of cross peaks could serve as a diagnostic tool for the comparison of different levels of electronic structure theory. By comparing frequency-domain RIXS and time-domain 1D-SXRS signals we show that the ability to probe electronic dynamics at different atomic centers is an advantage of the time-domain technique. 2D-SXRS offers a greater number of pulse combinations, and greater control over the preparation and measurement of electronic wavepackets.

The 1D-SXRS signal can be decomposed into the overlap of a doorway with a window wavepacket in Hilbert space. As discussed in Sec. III, the 2D-SXRS experiment can be written as the sum of two valence wavepacket overlaps. More detailed analysis of this signal is needed to relate these terms to valence electronic dynamics. Stimulated Raman techniques in the x-ray frequency range will allow many new and interesting measurements to be performed. 2D-SXRS provides a new window into the correlated valence electronic dynamics made possible by new x-ray sources.

APPENDIX A: THE EFFECTIVE TRANSITION POLARIZABILITY FOR GAUSSIAN PULSES

The effective polarizability has a simple form when the pulses have Gaussian envelopes. Assume the pulse envelopes are

$$\mathcal{E}_j(t) = e^{-t^2/2\sigma_j^2 - \phi_j}, \tag{A1}$$

where σ_j is the temporal pulse width (equal to intensity FWHM divided by $2\sqrt{\ln 2}$), which determines the bandwidth of the jth pulse. Inserting this definition into the time-domain

expression for the polarizability (Eq. (4)), we get

$$\alpha_{j;g'g''} = -i \sum_e V_{g'e} V_{eg''} \int_{-\infty}^{\infty} d\tau_2 \int_{-\infty}^{\tau_2} d\tau_1$$

$$\times \exp\left(-\frac{\tau_2^2}{2\sigma_j^2} - \frac{\tau_1^2}{2\sigma_j^2} + i\Delta_{eg'}^j \tau_2 - i\Delta_{eg''}^j \tau_1\right). \tag{A2}$$

Defining $\tau = \tau_2 - \tau_1$ allows us to write

$$\alpha_{j;g'g''} = -i \sum_e V_{g'e} V_{eg''} \int_0^{\infty} d\tau \exp\left(-\tau^2/2\sigma_j^2 + i\Delta_{eg'}^j \tau\right)$$

$$\times \int_{-\infty}^{\infty} d\tau_1 \exp\left(-(\tau_1^2 + \tau\tau_1)/\sigma_j^2 - i(\Delta_{eg''}^j - \Delta_{eg'}^j)\tau_1\right). \tag{A3}$$

The τ_1 integral can be easily done by switching to polar coordinates, and invoking the identity

$$\int_{-\infty}^{\infty} dt\, e^{-t^2} = \sqrt{\pi} \tag{A4}$$

to get

$$\alpha_{j;g'g''} = -i \sum_e V_{g'e} V_{eg''} \sqrt{\pi}\sigma_j \exp\left(-\left(\Delta_{eg''}^j - \Delta_{eg'}^j\right)^2 \sigma_j^2/4\right)$$

$$\times \int_0^{\infty} d\tau \exp\left(-\tau^2/4\sigma_j^2 + i\left(\Delta_{eg'}^j + \Delta_{eg''}^j\right)\tau/2\right). \tag{A5}$$

This integral can be written in terms of the complementary error function,

$$\int_z^{\infty} dt\, e^{-t^2} = \frac{\sqrt{\pi}}{2}\mathrm{erfc}(z). \tag{A6}$$

Substituting Eq. (A6) into Eq. (A5) gives

$$\alpha_{j;g'g''} = -i \sum_b V_{g'e} V_{eg''} \pi\sigma_j^2$$

$$\times \exp\left(-\sigma_j^2 \frac{\left(\Delta_{eg''}^j - \Delta_{eg'}^j\right)^2 + \left(\Delta_{eg''}^j + \Delta_{eg'}^j\right)^2}{4}\right)$$

$$\times \mathrm{erfc}\left(-i\sigma_j \frac{\Delta_{eg''}^j + \Delta_{eg'}^j}{2}\right), \tag{A7}$$

which can be simplified further to give Eq. (7).

APPENDIX B: ROTATIONALLY AVERAGED ALL-PARALLEL 2D-SXRS SIGNAL

Here we give the all-parallel 2D-SXRS signal as a tensor contraction over the polarization dependent expression

$$\mathbb{S}^{2D}(t_1, t_2) = \Im[\mathbb{S}_i(t_1, t_2) + \mathbb{S}_{ii}(t_1, t_2) + \mathbb{S}_{iii}(t_1, t_2)$$

$$+ \mathbb{S}_{iv}(t_1, t_2)], \tag{B1}$$

where $\mathbb{S}^{2D}$ is the sum of four terms (see Fig. 2):

$$\mathbb{S}_i(t_1, t_2) = -\langle \alpha_2^\dagger(t_2)\alpha_3(t_2 + t_1)\alpha_1(0)\rangle$$

$$= -\sum_{g'g''} \alpha_{2;gg'}^{\nu_3\nu_4*} \alpha_{3;g''g'}^{\nu_6\nu_5}$$

$$\times \alpha_{1;g'g}^{\nu_2\nu_1} e^{-i(\epsilon_{g'} - i\gamma_{g'})(t_1+t_2)} e^{+i(\epsilon_{g''} + i\gamma_{g''})t_2}, \tag{B2}$$

$$\mathbb{S}_{ii}(t_1, t_2) = \langle \alpha_1^\dagger(0)\alpha_2^\dagger(t_1)\alpha_3(t_1 + t_2)\rangle$$

$$= \sum_{g'g''} \alpha_{1;gg'}^{\nu_1\nu_2*} \alpha_{2;g'g''}^{\nu_3\nu_4*} \alpha_{3;g''g}^{\nu_6\nu_5} e^{+i(\epsilon_{g'} + i\gamma_{g'})t_1} e^{+i(\epsilon_{g''} + i\gamma_{g''})t_2}, \tag{B3}$$

$$\mathbb{S}_{iii}(t_1, t_2) = -\langle \alpha_1^\dagger(0)\alpha_3(t_1 + t_2)\alpha_2(t_1)\rangle$$

$$= -\sum_{g'g''} \alpha_{1;gg'}^{\nu_1\nu_2*} \alpha_{3;g'g''}^{\nu_6\nu_5}$$

$$\times \alpha_{2;g''g}^{\nu_4\nu_3} e^{+i(\epsilon_{g'} + i\gamma_{g'})(t_1+t_2)} e^{-i(\epsilon_{g''} - i\gamma_{g''})t_2}, \tag{B4}$$

$$\mathbb{S}_{iv}(t_1, t_2) = \langle \alpha_3(t_2 + t_1)\alpha_2(t_1)\alpha_1(0)\rangle$$

$$= \sum_{g'g''} \alpha_{3;gg''}^{\nu_6\nu_5} \alpha_{2;g''g'}^{\nu_4\nu_3} \alpha_{1;g'g}^{\nu_2\nu_1} e^{-i(\epsilon_{g'} - i\gamma_{g'})t_1} e^{-i(\epsilon_{g''} - i\gamma_{g''})t_2}. \tag{B5}$$

The parallel signal is found by contracting the tensor signal $\mathbb{S}_{\nu_1...\nu_6}^{2D}(t_1, t_2)$

$$\mathbb{S}_{\parallel}^{2D}(t_1, t_2) = \sum_{\nu_1...\nu_6} I_{\nu_1...\nu_6}^{\parallel} \mathbb{S}_{\nu_1...\nu_6}^{2D}(t_1, t_2) \tag{B6}$$

with the 12th-order isotropic tensor[57]

$$I_{\nu_1\nu_2\nu_3\nu_4\nu_5\nu_6}^{\parallel} = \frac{1}{105}\left(\delta_{\nu_1\nu_2}\delta_{\nu_3\nu_4}\delta_{\nu_5\nu_6} + \delta_{\nu_1\nu_2}\delta_{\nu_3\nu_5}\delta_{\nu_4\nu_6}\right.$$

$$+ \delta_{\nu_1\nu_2}\delta_{\nu_3\nu_6}\delta_{\nu_4\nu_5} + \delta_{\nu_1\nu_3}\delta_{\nu_2\nu_4}\delta_{\nu_5\nu_6}$$

$$+ \delta_{\nu_1\nu_3}\delta_{\nu_2\nu_5}\delta_{\nu_4\nu_6} + \delta_{\nu_1\nu_3}\delta_{\nu_2\nu_6}\delta_{\nu_4\nu_5}$$

$$+ \delta_{\nu_1\nu_4}\delta_{\nu_2\nu_3}\delta_{\nu_5\nu_6} + \delta_{\nu_1\nu_4}\delta_{\nu_2\nu_5}\delta_{\nu_3\nu_6}$$

$$+ \delta_{\nu_1\nu_4}\delta_{\nu_2\nu_6}\delta_{\nu_3\nu_5} + \delta_{\nu_1\nu_5}\delta_{\nu_2\nu_3}\delta_{\nu_4\nu_6}$$

$$+ \delta_{\nu_1\nu_5}\delta_{\nu_2\nu_4}\delta_{\nu_3\nu_6} + \delta_{\nu_1\nu_5}\delta_{\nu_2\nu_6}\delta_{\nu_3\nu_4}$$

$$+ \delta_{\nu_1\nu_6}\delta_{\nu_2\nu_3}\delta_{\nu_4\nu_5} + \delta_{\nu_1\nu_6}\delta_{\nu_2\nu_4}\delta_{\nu_3\nu_5}$$

$$\left.+ \delta_{\nu_1\nu_6}\delta_{\nu_2\nu_5}\delta_{\nu_3\nu_4}\right). \tag{B7}$$

[1] J. Marangos, "Introduction to the new science with x-ray free electron lasers," Contemp. Phys. **52**, 551 (2011).

[2] T. Popmintchev, M. Chen, P. Arpin, M. M. Murnane, and H. C. Kapteyn, "The attosecond nonlinear optics of bright coherent x-ray generation," Nat. Photonics **4**, 822 (2010).

[3] B. Adams, *Nonlinear Optics, Quantum Optics, and Ultrafast Phenomena with X-Rays* (Springer, 2003).

[4] S. Tanaka and S. Mukamel, "Probing exciton dynamics using Raman resonances in femtosecond x-ray four-wave mixing," Phys. Rev. A **67**, 033818 (2003).

[5] S. Mukamel, *Principles of Nonlinear Optical Spectroscopy* (Oxford University Press, New York, 1995).

[6]*XXII International Conference on Raman Spectroscopy (ICORS 2010)*, edited by P. Champion and L. Ziegler (American Institute of Physics, 2010).

[7]G. Eckhardt, R. W. Hellwarth, F. J. McClung, S. E. Schwarz, D. Weiner, and E. J. Woodbury, "Stimulated Raman scattering from organic liquids," Phys. Rev. Lett. **9**, 455 (1962).

[8]N. Bloembergen, "The stimulated Raman effect," Am. J. Phys. **35**, 989 (1967).

[9]A. Penzkofer, A. Laubereau, and W. Kaiser, "High intensity Raman interactions," Prog. Quantum Electron. **6**, 55 (1979).

[10]S. Mukamel and Y. J. Yan, "Manipulation of molecular motions using femtosecond pulse sequences," J. Phys. Chem. **95**, 1015 (1991).

[11]P. C. Becker, H. L. Fragnito, J. Y. Bigot, C. H. Brito Cruz, R. L. Fork, and C. V. Shank, "Femtosecond photon echoes from molecules in solution," Phys. Rev. Lett. **63**, 505 (1989).

[12]M. J. Rosker, F. W. Wise, and C. L. Tang, "Femtosecond relaxation dynamics of large molecules," Phys. Rev. Lett. **57**, 321 (1986).

[13]A. M. Weiner, S. D. Silvestri, and E. P. Ippen, "Three-pulse scattering for femtosecond dephasing studies: theory and experiment," J. Opt. Soc. Am. B **2**, 654 (1985).

[14]L. Dhar, J. A. Rogers, and K. A. Nelson, "Time-resolved vibrational spectroscopy in the impulsive limit," Chem. Rev. **94**, 157 (1994).

[15]J. D. Biggs and J. A. Cina, "Using wave-packet interferometry to monitor the external vibrational control of electronic excitation transfer," J. Chem. Phys. **131**, 224101 (2009).

[16]A. H. Zewail, "Femtochemistry: Atomic-scale dynamics of the chemical bond," J. Phys. Chem. A **104**, 5660 (2000).

[17]Y. Tanimura and S. Mukamel, "Two-dimensional femtosecond vibrational spectroscopy of liquids," J. Chem. Phys. **99**, 9496 (1993).

[18]B. W. J. McNeil and N. R. Thompson, "X-ray free-electron lasers," Nat. Photonics **4**, 814 (2010).

[19]P. Luchini and H. Motz, *Undulators and Free-electron Lasers* (Oxford University Press, New York, 1990).

[20]LCLS Scientific Advisory Committee and LCLS Technical Advisory Committee, *LCLS: The First Experiments* (Stanford Linear Accelerator Center of Stanford University, 2000).

[21]P. Emma, R. Akre, J. Arthur, R. Bionta, C. Bostedt, J. Bozek, A. Brachmann, P. Bucksbaum, R. Coffee, F. J. Decker, Y. Ding, D. Dowell, S. Edstrom, A. Fisher, J. Frisch, S. Gilevich, G. Hastings, G. Hays, P. Hering, Z. Huang, R. Iverson, H. Loos, M. Messerschmidt, A. Miahnahri, S. Moeller, H. D. Nuhn, G. Pile, D. Ratner, J. Rzepiela, D. Schultz, T. Smith, P. Stefan, H. Tompkins, J. Turner, J. Welch, W. White, J. Wu, G. Yocky, and J. Galayda, "First lasing and operation of an angstrom-wavelength free-electron laser," Nat. Photonics **4**, 641 (2010).

[22]S. M. Vinko, O. Ciricosta, B. I. Cho, K. Engelhorn, H. Chung, C. R.D. Brown, T. Burian, J. Chalupsky, R. W. Falcone, C. Graves, V. Hajkova, A. Higginbotham, L. Juha, J. Krzywinski, H. J. Lee, M. Messerschmidt, C. D. Murphy, Y. Ping, A. Scherz, W. Schlotter, S. Toleikis, J. J. Turner, L. Vysin, T. Wang, B. Wu, U. Zastrau, D. Zhu, R. W. Lee, P. A. Heimann, B. Nagler, and J. S. Wark, "Creation and diagnosis of a solid-density plasma with an x-ray free-electron laser," Nature (London) **482**, 59 (2012).

[23]R. Neutze, R. Wouts, D. van der Spoel, E. Weckert, and J. Hajdu, "Potential for biomolecular imaging with femtosecond x-ray pulses," Nature (London) **406**, 752 (2000).

[24]H. M. Quiney and K. A. Nugent, "Biomolecular imaging and electronic damage using x-ray free-electron lasers," Nat. Phys. **7**, 142 (2011).

[25]L. Young, E. P. Kanter, B. Krässig, Y. Li, A. M. March, S. T. Pratt, R. Santra, S. H. Southworth, N. Rohringer, L. F. DiMauro, G. Doumy, C. A. Roedig, N. Berrah, L. Fang, M. Hoener, P. H. Bucksbaum, J. P. Cryan, S. Ghimire, J. M. Glownia, D. A. Reis, J. D. Bozek, C. Bostedt, and M. Messerschmidt, "Femtosecond electronic response of atoms to ultra-intense x-rays," Nature (London) **466**, 56 (2010).

[26]M. Hoener, L. Fang, O. Kornilov, O. Gessner, S. T. Pratt, M. Gühr, E. P. Kanter, C. Blaga, C. Bostedt, J. D. Bozek, P. H. Bucksbaum, C. Buth, M. Chen, R. Coffee, J. Cryan, L. DiMauro, M. Glownia, E. Hosler, E. Kukk, S. R. Leone, B. McFarland, M. Messerschmidt, B. Murphy, V. Petrovic, D. Rolles, and N. Berrah, "Ultraintense X-Ray induced ionization, dissociation, and frustrated absorption in molecular nitrogen," Phys. Rev. Lett. **104**, 253002 (2010).

[27]C. Gutt, P. Wochner, B. Fischer, H. Conrad, M. Castro-Colin, S. Lee, F. Lehmkühler, I. Steinke, M. Sprung, W. Roseker, D. Zhu, H. Lemke, S. Bogle, P. H. Fuoss, G. B. Stephenson, M. Cammarata, D. M. Fritz, A. Robert, and G. Grübel, "Single shot spatial and temporal coherence proper-

ties of the slac linac coherent light source in the hard x-ray regime," Phys. Rev. Lett. **108**, 024801 (2012).

[28]N. Rohringer, D. Ryan, R. A. London, M. Purvis, F. Albert, J. Dunn, J. D. Bozek, C. Bostedt, A. Graf, R. Hill, S. P. Hau-Riege, and J. J. Rocca, "Atomic inner-shell x-ray laser at 1.46 nanometres pumped by an x-ray free-electron laser," Nature (London) **481**, 488 (2012).

[29]P. M. Rentzepis, "Direct measurements of radiationless transitions in liquids," Chem. Phys. Lett. **2**, 117 (1968).

[30]J. W. Gadzuk, "Core level spectroscopy: A dynamics perspective," Phys. Scr. **35**, 171 (1987).

[31]N. Rohringer and R. Santra, "X-ray nonlinear optical processes using a self-amplified spontaneous emission free-electron laser," Phys. Rev. A **76**, 033416 (2007).

[32]J. M. Glownia, J. Cryan, J. Andreasson, A. Belkacem, N. Berrah, C. I. Blaga, C. Bostedt, J. Bozek, L. F. DiMauro, L. Fang, J. Frisch, O. Gessner, M. G?hr, J. Hajdu, M. P. Hertlein, M. Hoener, G. Huang, O. Kornilov, J. P. Marangos, A. M. March, B. K. McFarland, H. Merdji, V. S. Petrovic, C. Raman, D. Ray, D. A. Reis, M. Trigo, J. L. White, W. White, R. Wilcox, L. Young, R. N. Coffee, and P. H. Bucksbaum, "Time-resolved pump-probe experiments at the LCLS," Opt. Express **18**, 17620 (2010).

[33]V. C. Felicíssimo, F. F. Guimarães, F. Gel'mukhanov, A. Cesar, and H. Ågren, "The principles of infrared-x-ray pump-probe spectroscopy. applications on proton transfer in core-ionized water dimers," J. Chem. Phys. **122**, 094319 (2005).

[34]F. F. Guimarães, F. Gel'mukhanov, A. Cesar, and H. Ågren, "Quantum wave packet revivals in IR + x-ray pumpprobe spectroscopy," Chem. Phys. Lett. **405**, 398 (2005).

[35]F. F. Guimarães and F. Gel'mukhanov, "Pump-probe spectroscopy of molecules driven by infrared field in both ground and excited electronic states," J. Chem. Phys. **125**, 204313 (2006).

[36]V. C. Felicíssimo, F. F. Guimarães, and F. Gel'mukhanov, "Enhancement of the recoil effect in x-ray photoelectron spectra of molecules driven by a strong ir field," Phys. Rev. A **72**, 023414 (2005).

[37]F. F. Guimarães, V. Kimberg, F. Gel'mukhanov, and H. Ågren, "Two-color phase-sensitive x-ray pump-probe spectroscopy," Phys. Rev. A **70**, 062504 (2004).

[38]F. Gel'mukhanov and H. Ågren, "Resonant x-ray Raman scattering," Phys. Rep. **312**, 87 (1999).

[39]J. Nordgren, G. Bray, S. Cramm, R. Nyholm, J. Rubensson, and N. Wassdahl, "Soft x-ray emission spectroscopy using monochromatized synchrotron radiation," Rev. Sci. Instrum. **60**, 1690 (1989).

[40]S. Tanaka and S. Mukamel, "Coherent x-ray Raman spectroscopy: A nonlinear local probe for electronic excitations," Phys. Rev. Lett. **89**, 043001 (2002).

[41]K. A. Nugent, "Coherent methods in the x-ray sciences," Adv. Phys. **59**, 1 (2010).

[42]B. Patterson, "Resource letter on stimulated inelastic x-ray scattering at an XFEL," Technical Report SLAC, 2010, see http://slac.stanford.edu/pubs/slactns/tn04/slac-tn-10-026.pdf.

[43]A. Zholents and G. Penn, "Obtaining two attosecond pulses for x-ray stimulated Raman spectroscopy," Nucl. Instrum. Methods A **612**, 254 (2010).

[44]A. I. Kuleff and L. S. Cederbaum, "Tracing ultrafast interatomic electronic decay processes in real time and space," Phys. Rev. Lett. **98**, 083201 (2007).

[45]E. Goulielmakis, Z. Loh, A. Wirth, R. Santra, N. Rohringer, V. S. Yakovlev, S. Zherebtsov, T. Pfeifer, A. M. Azzeer, M. F. Kling, S. R. Leone, and F. Krausz, "Real-time observation of valence electron motion," Nature (London) **466**, 739 (2010).

[46]F. Reiter, U. Graf, E. E. Serebryannikov, W. Schweinberger, M. Fiess, M. Schultze, A. M. Azzeer, R. Kienberger, F. Krausz, A. M. Zheltikov, and E. Goulielmakis, "Route to attosecond nonlinear spectroscopy," Phys. Rev. Lett. **105**, 243902 (2010).

[47]P. Tzallas, E. Skantzakis, L. A. A. Nikolopoulos, G. D. Tsakiris, and D. Charalambidis, "Extreme-ultraviolet pump-probe studies of one-femtosecond-scale electron dynamics," Nat. Phys. **7**, 781 (2011).

[48]S. Tanaka, S. Volkov, and S. Mukamel, "Time-resolved x-ray Raman spectroscopy of photoexcited polydiacetylene oligomer: A simulation study," J. Chem. Phys. **118**, 3065 (2003).

[49]S. Mukamel and H. Wang, "Manipulating quantum entanglement of quasi-particles in many-electron systems by attosecond x-ray pulses," Phys. Rev. A **81**, 062334 (2010).

[50]S. Rahav, O. Roslyak, and S. Mukamel, "Manipulating stimulated coherent anti-Stokes Raman spectroscopy signals by broad-band and narrow-band pulses," J. Chem. Phys. **131**, 194510 (2009).

[51] U. Harbola and S. Mukamel, "Coherent stimulated x-ray Raman spectroscopy: Attosecond extension of resonant inelastic x-ray Raman scattering," Phys. Rev. B **79**, 085108 (2009).

[52] I. V. Schweigert and S. Mukamel, "Probing valence electronic wave-packet dynamics by all x-ray stimulated raman spectroscopy: A simulation study," Phys. Rev. A **76**, 012504 (2007).

[53] D. Healion, H. Wang, and S. Mukamel, "Simulation and visualization of attosecond stimulated x-ray Raman spectroscopy signals in trans-N-methylacetamide at the nitrogen and oxygen k-edges," J. Chem. Phys. **134**, 124101 (2011).

[54] G. Zschornack, *Handbook of X-ray Data* (Springer-Verlag, Berlin, 2007).

[55] S. Mukamel and S. Rahav, in *Advances in Atomic, Molecular and Optical Physics* (Academic, 2010), Vol. 59, pp. 223–263.

[56] J. D. Biggs, J. A. Voll, and S. Mukamel, "Coherent nonlinear optical studies of elementary processes in biological complexes; diagrammatic techniques based on the wavefunction vs. the density matrix," Philos. Trans. R. Soc. London, Ser. A (2012), doi:10.1098/rsta.2011.0219.

[57] D. L. Andrews and T. Thirunamachandran, "On three-dimensional rotational averages," J. Chem. Phys. **67**, 5026 (1977).

[58] S. Rahav and S. Mukamel, "Multidimensional attosecond photoelectron spectroscopy with shaped pulses and quantum optical fields," Phys. Rev. A **81**, (2010).

[59] D. V. Voronine, D. Abramavicius, and S. Mukamel, "Manipulating multidimensional electronic spectra of excitons by polarization pulse shaping," J. Chem. Phys. **126**, 044508 (2007).

[60] S. Zhang, H. Zhang, T. Jia, Z. Wang, and Z. Sun, "Selective excitation of femtosecond coherent anti-Stokes Raman scattering in the mixture by phase-modulated pump and probe pulses," J. Chem. Phys. **132**, 044505 (2010).

[61] J. Roslund, O. M. Shir, A. Dogariu, R. Miles, and H. Rabitz, "Control of nitromethane photoionization efficiency with shaped femtosecond pulses," J. Chem. Phys. **134**, 154301 (2011).

[62] The effective polarizability is proportional to the second-order reduced pulse propagator described in Ref. 15.

[63] R. Send, M. Kühn, and F. Furche, "Assessing excited state methods by adiabatic excitation energies," J. Chem. Theory Comput. **7**, 2376 (2011).

[64] Y. Zhang, J. Biggs, D. Healion, N. Govind, and S. Mukamel (unpublished).

[65] M. J. Frisch, G. W. Trucks, H. B. Schlegel *et al.*, GAUSSIAN 09, Revision A.1 (Gaussian, Inc., Wallingford, CT, 2009).

[66] W. J. Hunt and W. A. Goddard III, "Excited states of H_2O using improved virtual orbitals," Chem. Phys. Lett. **3**, 414 (1969).

[67] H. Ågren, V. Carravetta, O. Vahtras, and L. G.M. Pettersson, "Direct, atomic orbital, static exchange calculations of photoabsorption spectra of large molecules and clusters," Chem. Phys. Lett. **222**, 75 (1994).

[68] H. Ågren, V. Carravetta, O. Vahtras, and L. G. M. Pettersson, "Direct scf direct static-exchange calculations of electronic spectra," Theor. Chem. Acc. **97**, 14 (1997).

[69] T. D. Crawford, C. D. Sherrill, E. Valeev, J. Fermann, R. King, M. Leininger, S. Brown, C. Janssen, E. Seidl, J. Kenny, and W. Allen, J. Comp. Chem. **28**, 1610 (2007).

[70] R. Martin, "Natural transition orbitals," J. Chem. Phys. **118**, 4775 (2003).

[71] K. Kaya and S. Nagakura, "Vacuum ultraviolet absorption spectra of simple amides," Theor. Chim. Acta **7**, 117 (1967).

[72] J. Bearden and A. Burr, "Reevaluation of X-ray atomic energy levels," Rev. Mod. Phys. **39**, 125 (1967).

[73] I. V. Schweigert and S. Mukamel, "Double-quantum-coherence attosecond x-ray spectroscopy of spatially separated, spectrally overlapping core-electron transitions," Phys. Rev. A **78**, 052509 (2008).

[74] J. van den Brink and M. van Veenendaal, "Correlation functions measured by indirect resonant inelastic x-ray scattering," Europhys. Lett. **73**, 121 (2006).

[75] L. J.P. Ament, M. van Veenendaal, T. P. Devereaux, J. P. Hill, and J. van den Brink, "Resonant inelastic x-ray scattering studies of elementary excitations," Rev. Mod. Phys. **83**, 705 (2011).

[76] F. Gel'mukhanov and H. Ågren, "Resonant inelastic x-ray scattering with symmetry-selective excitation," Phys. Rev. A **49**, 4378 (1994).

[77] P. Glatzel, U. Bergmann, J. Yano, H. Visser, J. H. Robblee, W. Gu, F. M. F. de Groot, G. Christou, V. L. Pecoraro, S. P. Cramer, and V. K. Yachandra, "The electronic structure of mn in oxides, coordination complexes, and the Oxygen-Evolving complex of photosystem II studied by resonant inelastic x-ray scattering," J. Am. Chem. Soc. **126**, 9946 (2004).

[78] F. de Groot and A. Kotani, *Core Level Spectroscopy of Solids*, 1st ed. (CRC, 2008).

[79] C. Fang, R. R. Frontiera, R. Tran, and R. A. Mathies, "Mapping GFP structure evolution during proton transfer with femtosecond raman spectroscopy," Nature (London) **462**, 200 (2009).

[80] P. Kukura, D. W. McCamant, and R. A. Mathies, "Femtosecond stimulated raman spectroscopy," Ann. Rev. Phys. Chem. **58**, 461 (2007).